Parametric Mössbauer radiation source

O. D. Skoromnik[1,*] I. D. Feranchuk[2,†] J. Evers[1] and C. H. Keitel[1]

[1]*Max Planck Institute for Nuclear Physics, Saupfercheckweg 1, 69117 Heidelberg, Germany*
[2]*Belarusian State University, 4 Nezavisimosty Avenue, 220030, Minsk, Belarus*

Numerous applications of Mössbauer spectroscopy are related to a unique resolution of absorption spectra of resonant radiation in crystals, when the nucleus absorbs a photon without a recoil. However, the narrow nuclear linewidth renders efficient driving of the nuclei challenging, restricting precision spectroscopy, nuclear inelastic scattering and nuclear quantum optics. Moreover, the need for dedicated x-ray optics restricts access to only few isotopes, impeding precision spectroscopy of a wider class of systems. Here, we put forward a novel Mössbauer source, which offers resonant photon flux for a large variety of Mössbauer isotopes with strongly suppressed electronic background. It is based on relativistic electrons moving through a crystal and emitting parametric Mössbauer radiation essentially unattenuated by electronic absorption. As a result, a collimated beam of resonant photons is formed, without the need for additional monochromatization. We envision the extension of high-precision Mössbauer spectroscopy to a wide range of isotopes at accelerator facilities, also using dumped electron beams.

I. INTRODUCTION

Traditional Mössbauer spectroscopy uses radioactive sources, which provide essentially background-free near-resonant γ radiation with a spectral width of the order of the natural linewidth of the involved nuclear transitions [1–9]. Accelerator-based x-ray sources offer orders of magnitude more resonant photon flux, but the short x-ray pulses contain an intense off-resonant background, which strongly exceeds the resonant component. As a result, Mössbauer spectroscopy usually is performed in the time domain [3,10], removing the "prompt" nonresonant background via temporal gating of the detectors. This, for instance, restricts the study of short-lived isotopes, for which the gating leads to a severe loss of signal photons due to the fast initial decay.

Alternatively, synchrotron Mössbauer sources (SMS) [11–15] can be employed to monochromatize the synchrotron radiation to few natural linewidths using pure nuclear Bragg reflexes, enabled by the suppression of electronic reflections via particular crystal symmetries. In addition, usually a specific Mössbauer isotope is targeted, requiring dedicated x-ray optics such as monochromators to reduce

the off-resonant background component. Therefore, it is challenging to make new Mössbauer isotopes accessible at modern pulsed x-ray sources, which hinders the exploration of new scientific applications of specific Mössbauer nuclei [2,16].

An alternative scheme to generate x rays is parametric x-ray radiation (PXR), based on relativistic electrons moving through a crystal [17–27]. In PXR, the electron self-field diffracts on the crystallographic planes, which leads to the generation of electromagnetic radiation. Its relative spectral and angular widths are suppressed by the large electron energy E, via the relativistic γ factor $\gamma = E/m_e c^2$, resulting in quasimonochromatic and well collimated PXR radiation. Moreover, it is possible to fix the electron angle of incidence in such a way that one of the PXR peaks is in resonance with a nuclear Mössbauer transition, giving rise to parametric Mössbauer radiation (PMR) [28].

However, conventional PXR schemes are limited in intensity due to substantial x-ray absorption in the crystal [28,29]. This can be understood by noting that the PXR intensity depends on the crystal polarizability [17,19]. For crystal diffraction, the polarizability is maximized near the resonance frequencies, where also the absorption becomes large. To overcome this issue, a particular geometry featuring extremely asymmetric diffraction (EAD) was suggested [30]. This geometry exploits a peculiar PXR feature, namely, that the radiation is emitted under a large angle relative to the electron velocity, which is in stark contrast with other mechanisms generating radiation from relativistic particles. In the EAD geometry, the electrons are moving in a thin crystal layer parallel to the crystal-vacuum interface in such a way that the emitted photons

*olegskor@gmail.com
†iferanchuk@gmail.com

immediately exit the crystal without much absorption. This effectively increases the intensity of the radiation by 2 orders of magnitude with respect to the conventional transition geometries. However, so far, EAD geometries have only been studied related to the generation of spectrally broad x rays, and not to spectrally narrow x rays as required for applications in Mössbauer science. *A priori*, it is not clear how an EAD-like condition could be applied to the PMR case.

Here, we put forward a novel versatile source for Mössbauer spectroscopy, which is based on PXR simultaneously satisfying the Mössbauer resonance condition to effectively excite the nuclei and the EAD condition to suppress absorption. In fact, we for the first time simultaneously combine a Mössbauer crystal with the EAD geometry. This source offers narrow-band nuclear resonant photon flux for a large variety of Mössbauer crystals, including those which do not offer a radioactive parent isotope. The possibility to operate the source in a nondedicated way, e.g., using dumped electron beams, opens perspectives for new experimental approaches with Mössbauer nuclei in particular for low-count rate or photon-hungry setups. We furthermore show that for certain crystals, SMS-like suppression of electronic scattering can simultaneously be met within the crystal generating the Mössbauer radiation, leading to the suppression of the off-resonant electronic background radiation. In this case, our calculations predict almost background-free emission of Mössbauer radiation, paving the way to Mössbauer spectroscopy on short-lived isotopes directly in the energy domain, without the need for additional time gating or the development of dedicated monochromatizers.

We illustrate our approach in the case of ^{121}Sb, for which our simulations predict essentially background-free emission. We further discuss two isotopes without the SMS condition: ^{133}Cs in order to illustrate the interplay between the electron and nuclear components of the crystal polarizabilities, and ^{57}Fe as the classical workhorse of Mössbauer spectroscopy. The total linewidth of a PMR source is $\sim$5–20 Γ depending on the crystal. Finally, we analyze ^{45}Sc which is of interest due to an extremely narrow linewidth $\sim 10^{-15}$ eV.

II. CALCULATION OF THE PMR SPECTRA

To calculate PXR and PMR, in the following we evaluate the differential number of photons $\partial N_{\omega s}/(\partial\omega\partial\Omega)$ emitted in the frequency interval $(\omega, \omega + d\omega)$ and in the solid angle $d\Omega$, following the approach in Refs. [17,18,31]. In short, we solve the inhomogeneous Maxwell's equations using a Green's function and the standard two-wave approximation approach of dynamical diffraction theory [32]. Finally, we use the such obtained electric field to calculate the energy- and angular-resolved PXR and PMR photon flux, first for a single electron, and then averaged over experimentally relevant electron distributions.

A. Solution of Maxwell's equations

We start the analysis from the inhomogeneous Maxwell's equations for the Fourier components of the fields, which contain the source current $j(r, t)$ generated by a charged particle [17]. In the case of PXR, the charged particle moves uniformly, i.e.,

$$r(t) = r_0 + vt, \tag{1}$$

where r_0 is the initial position at $t = 0$. The displacement field $D(r, \omega)$ is related to the electric field $E(r, \omega)$ through the permittivity tensor $\epsilon_{\alpha\beta}(r, r_1, \omega)$, which is defined in the whole space, but has different expressions inside the crystal and outside, in vacuum. To facilitate the calculation, we expand the permittivity inside the crystal in a series over the reciprocal lattice vectors g.

After this, the Green's function for Maxwell's equations is defined as

$$\varepsilon_{\alpha\beta\gamma}\varepsilon_{\gamma\mu\nu}\frac{\partial^2}{\partial x_\beta\partial x_\mu}G_{\nu\lambda}(r, r', \omega)$$
$$-\frac{\omega^2}{c^2}\int dr_1\,\epsilon_{\alpha\beta}G_{\beta\lambda}(r_1, r', \omega) = \delta_{\alpha\lambda}\delta(r - r'), \tag{2}$$

where $\varepsilon_{\alpha\beta\gamma}$ and $\varepsilon_{\gamma\mu\nu}$ are Levi-Civita symbols. In the far-field limit $r \gg r'$, the Green's function can be expressed through the solution $E_{k's}^{(-)}$ of the homogeneous Maxwell's equations as

$$G_{\alpha\beta}(r, r', \omega) \approx \frac{e^{ikr}}{4\pi r}\sum_{s=1,2}e_\alpha^{(s)}E_{k'\beta s}^{(-)*}(r', \omega), \tag{3}$$

where s is a polarization index. Then, this Green's function is used to determine the field generated by the current via

$$E_\alpha(r, \omega) = i\omega\frac{4\pi}{c}\int dr'\,G_{\alpha\beta}(r, r', \omega)\,j_\beta(r', \omega). \tag{4}$$

Finally, this field is then used in the standard expression for the energy density via the Poynting vector

$$W_{n\omega} = \frac{cr^2}{4\pi^2}|E(r, t)|^2 \tag{5}$$

of the scattered light. Here, n is the unit vector in the observation direction. The result is

$$\frac{\partial^2 N_{n,\omega s}}{\partial\omega\partial\Omega} = \frac{e_0^2\omega}{4\pi^2\hbar c^3}\left|\int E_{k's}^{(-)*}[r(t), \omega]\cdot v(t)e^{i\omega t}dt\right|^2, \tag{6}$$

where $k' = kr/r$ points in observation direction.

It is important to note that the solution $E_{ks}^{(-)}$ of the homogeneous Maxwell's equations possesses an asymptotic behavior for large $|r|$ as a plane wave and an ingoing

spherical wave. In contrast, when an external electromagnetic field $E_{ks}^{(+)}$ is diffracted or scattered on a crystal, it has an asymptotic behavior of a plane wave and an outgoing spherical wave. However, these two field configurations are related to each other by the reciprocity theorem [33] $E_{ks}^{(-)} = E_{-ks}^{(+)*}$. Thus, the actual problem is reduced to the solution of the diffraction problem to find the field $E_{ks}^{(+)}$, the usage of the reciprocity theorem, and the subsequent application of Eq. (6). For this reason, the actual vector of the emitted photon k' is related to the vector k of the diffraction problem via $k' = -k$.

B. Solution of the diffraction problem

1. Two-wave approximation

In order to determine the electric field in Eq. (6), the diffraction problem is solved within the two-wave approximation of the dynamical diffraction theory [32], which is valid if only two strong electromagnetic waves are excited in the crystal. The amplitudes of these waves satisfy a set of homogeneous algebraic equations:

$$\left(\frac{k^2}{k_0^2} - 1 - \chi_0\right)E_{ks} - c_s\chi_{-g}E_{k_gs} = 0,$$

$$\left(\frac{k_g^2}{k_0^2} - 1 - \chi_0\right)E_{k_gs} - c_s\chi_g E_{ks} = 0, \tag{7}$$

where $k_0 = \omega/c$, the incident wave $E_{ks}^{(+)} = e_s E_{ks}$ and the diffracted wave $E_{k_gs}^{(+)} = e_{1s}E_{k_gs}$. Here e_s and e_{1s} are the unit vectors of σ and π polarizations [32]. A nontrivial solution of this linear homogeneous equation system exists, if the corresponding determinant is vanishing. This condition determines the dispersion relation, and its solutions ε_{1s} and ε_{2s} fix the wave vectors

$$k_{1,2s} = k_0 n - k_0 \varepsilon_{1,2s} N \tag{8}$$

of the diffracted waves. Having found the solutions of the dispersion equation, one writes down Maxwell's equations in the crystal and in vacuum and exploits the continuity of the fields at the crystal-vacuum interface. This fixes the amplitudes of all waves. In particular, the electromagnetic field responsible for the formation of PMR equals

$$E_{ks}^{(+)} = e_{1s}E_{g1s}e^{ik_g \cdot r - ik_0 z \varepsilon_{1s}}, \tag{9}$$

$$E_{g1s} = \frac{c_s\chi_g}{\alpha_B + \chi_0}. \tag{10}$$

We further find that the wave vector k' corresponding to the maximum PXR as well as PMR emission direction (see Fig. 1) is determined as a solution of two equations: (a) the Cherenkov radiation condition [18]

$$q' = \text{Re } q = 1 + \frac{(k+g) \cdot v}{\omega_0} = 0 \tag{11}$$

for the diffracted wave and (b) minimal value for the deviation from Wulff-Bragg's condition [17–19]

$$|\alpha_B| = \frac{|(k+g)^2 - k^2|}{|k|^2} = \frac{|2k \cdot g + g^2|}{|k|^2}. \tag{12}$$

The latter condition describes the diffraction of an electron self-field on the crystallographic planes with the reciprocal lattice vector $g = (g_x, g_y, g_z)$, where v is the electron velocity and $|k| = \omega_0/c$ with ω_0 the frequency of the resonant Mössbauer transition. Note that due to the reciprocity theorem the calculation of the radiation intensity is based on the solutions of the Maxwell equations with the reversed wave vector $k = -k'$.

2. EAD geometry

Next, we consider the EAD geometry case [30,31], see Fig. 1, in which electrons are moving parallel to the crystal-vacuum interface (parallel to the x-y plane) and emit radiation under a large angle to the crystal surface. In this geometry, the angle ψ_0 between $g_\perp$ and the electron velocity v we adjust in such a way that the frequency of the emitted radiation is coincident with the resonance frequency of the Mössbauer isotope.

Solving Eqs. (11) and (12) under the condition $k_g \cdot N = (k+g) \cdot N = 0$, which specifies the EAD geometry, we find that the maximum of the x-ray emission is in the direction

$$k' = -k = (g_x + \omega_0/v, g_y, g_z). \tag{13}$$

The z component causes the generated radiation to immediately leave the crystal, such that absorption within the crystal is greatly reduced. The resonance condition

$$k^2 = (\omega_0/c)^2 = k_0^2 \tag{14}$$

yields

$$\cos \psi_0 = -\frac{v}{k_0 c}\frac{k_0^2\gamma^{-2} + g^2}{2\sqrt{g^2 - g_z^2}}. \tag{15}$$

C. Integration over the trajectory of a single electron

Next, we insert the solution of the diffraction problem for the electric field into Eq. (6). The integration over the particle trajectory in Eq. (6) for the linear motion of constant velocity yields
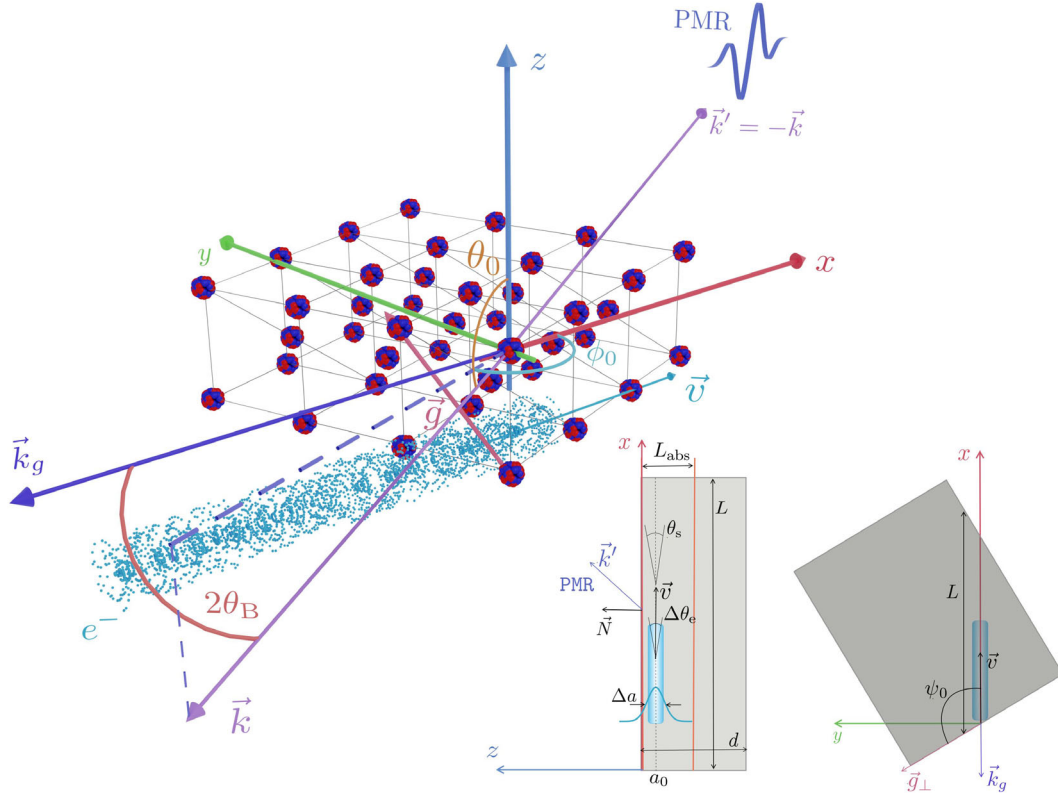
FIG. 1.   Schematic setup for the generation of PMR in the EAD geometry. The electron beam moves uniformly with velocity $\boldsymbol{v}$ in the x direction. The crystal surface lies in the x-y plane. $\boldsymbol{g}$ is the reciprocal crystal lattice vector. PMR will be mainly emitted in the direction given by the vector $\boldsymbol{k}' = -\boldsymbol{k} = -k_0(\sin\theta_0 \cos\phi_0, \sin\theta_0 \sin\phi_0, \cos\theta_0)$, and thus rapidly leaves the crystal without significant electronic absorption. $\boldsymbol{k}_g = \boldsymbol{k} + \boldsymbol{g}$ and θ_{B} is the Bragg angle. The energy of the PXR is tuned using the angle ψ_0 between the electron velocity and the projection $\boldsymbol{g}_\perp$ of $\boldsymbol{g}$ on the crystal surface.

$$\frac{\partial^2 N_{\boldsymbol{n},\omega s}}{\partial\omega\partial\Omega} = \frac{e_0^2 \omega}{4\pi^2 \hbar c^5} \sum_{s=\sigma,\pi} (\boldsymbol{e}_{1s} \cdot \boldsymbol{v})^2$$

$$\times |E_{g1s} L_g (1 - e^{-iL/L_g})|^2 e^{-2k_0|\varepsilon''_{1s} z_0|}, \qquad (16)$$

where $L_g = 1/(k_0 q)$ is the coherence length and $q = 1 + (\boldsymbol{k}_g \cdot \boldsymbol{v})/\omega_0 - \varepsilon_{1s} v_z/c$.

D. Integration over emission angles

In order to fix a coordinate system and to determine the direction of the x-ray emission, we for the moment consider an ideal case, in which the electron velocity does not have any component in the transverse direction and the minimum of Bragg's condition Eq. (12) is reached, i.e., $\alpha_{\mathrm{B}} = \gamma^{-2}$. We align the x axis parallel to the electron velocity, and the z axis along the normal $\boldsymbol{N}$ to the crystal surface. In this geometry, the incident electron beam, as well as the diffracted wave with vector $\boldsymbol{k}_g = \boldsymbol{k} + \boldsymbol{g}$, both propagate along the crystal surface [31], such that $\boldsymbol{k}_g \cdot \boldsymbol{N} = 0$. For a given Bragg reflex, we denote the projection of the corresponding reciprocal lattice vector $\boldsymbol{g}$ onto the x-y plane by $\boldsymbol{g}_\perp$.

The remaining task is to determine the deviations from the Cherenkov radiation condition $q' = \mathrm{Re}\, q = 0$ and the deviation α_{B} from the Bragg's diffraction condition for nonideal particle velocities. For this, we consider electrons with velocities deviating from the ideal velocity $\boldsymbol{v}_0 = v\boldsymbol{e}_x$. We parametrize these deviations via $\boldsymbol{v} = v(\cos\theta_e \boldsymbol{e}_x + \boldsymbol{\theta}_e)$, with $\boldsymbol{\theta}_e = (0, \theta_{ey}, \theta_{ez})$ and $\theta_e^2 = \theta_{ey}^2 + \theta_{ez}^2$. Analogously, the wave vector of the emitted radiation $\boldsymbol{k} = k_0(\sin\theta\cos\phi, \sin\theta\sin\phi, \cos\theta)$ will acquire deviations from its ideal direction $\boldsymbol{k}_0$. In order to determine these deviations, we expand the angular dependence in a Taylor series around the ideal direction θ_0 and ϕ_0 up to second order, i.e., $\boldsymbol{k} = \boldsymbol{k}_0 + \boldsymbol{u}_1 + \boldsymbol{u}_2$; $\boldsymbol{k}^2 = k_0^2$; $\boldsymbol{k}_0 \cdot \boldsymbol{u}_1 = 0$. As a result of the deviations from the ideal directions, the quantities q' and α_{B} will exhibit corresponding variations

$$q' = (\theta - \theta_0)\cos\theta_0 \cos\phi_0 - (\phi - \phi_0)\sin\theta_0 \sin\phi_0,$$

$$(17)$$

$$\alpha_{\mathrm{B}} = -\{\gamma^{-2} + [\theta_{ez} - (\theta - \theta_0)\sin\theta_0]^2 + [\theta_{ey} + (\phi - \phi_0)\sin\theta_0 \cos\phi_0 + (\theta - \theta_0)\cos\theta_0 \sin\phi_0]^2\}. \qquad (18)$$

The integration over the x-ray emission angles with respect to ϕ is performed in the following manner. First, we apply a variable change $\phi - \phi_0 \to q'$. Second, we exploit the fact that the distribution function is sharply peaked near $\phi = \phi_0$, which allows us to extend the integration range from $[-\phi_0, 2\pi - \phi_0]$ to the interval $(-\infty, \infty)$. Third, since the imaginary part of q is much smaller than its real part, we can simplify its evaluation by using the value ϕ for the maximum of the intensity. This intensity maximum is located at $q' = 0$, which fixes the relation between θ and ϕ. Thus, we substitute $\phi - \phi_0 = (\theta - \theta_0) \cot \theta_0 \cot \phi_0$ in the imaginary part of q. Finally, we perform the integration with the help of the residue theorem yielding Eq. (19).

In addition, it is important to note that the electron velocity spread in the transversal y direction, which is typically [34] much larger than the corresponding spread in the z direction, does not influence the emitted number of photons. This is due to the independence of the photon distribution function of the initial position y_0 of the electron for the case of the EAD geometry.

III. DISTRIBUTION OF EMITTED PHOTONS

The integration over the particle trajectory and over the x-ray spherical emission angle ϕ yields the spectral-angular distribution of the emitted photons

$$\frac{\partial^2 N}{\partial \omega \partial \theta} = \frac{e_0^2}{4\pi\hbar c\omega} \frac{1}{|\sin \phi_0|} \sum_{s=\sigma,\pi} \left[|E_{g1s}|^2 \left(\frac{\boldsymbol{v} \cdot \boldsymbol{e}_{1s}}{c} \right)^2 \right.$$
$$\left. \times \frac{1 - e^{-2k_0 L q_s''}}{q_s''} e^{-2k_0 |z_0 \varepsilon_{1s}''|} \right], \quad (19)$$

where L is the crystal length, z_0 is the electron initial coordinate, and

$$E_{g1s} = \frac{c_s \chi_g}{\alpha_B + \chi_0} \quad (20)$$

is the amplitude of the diffracted wave. The index s sums over the σ and π polarizations, with $c_\sigma = 1$ and $c_\pi = \cos 2\theta_B$, and polarization vectors

$$\boldsymbol{e}_{1\sigma} = \boldsymbol{k} \times \boldsymbol{g} / |\boldsymbol{k} \times \boldsymbol{g}|, \quad (21)$$

$$\boldsymbol{e}_{1\pi} = \boldsymbol{k}_g \times \boldsymbol{e}_{1\sigma} / |\boldsymbol{k}_g \times \boldsymbol{e}_{1\sigma}|. \quad (22)$$

Finally, $q_s'' = |\theta_{ez} \varepsilon_{1s}''|$, where θ_{ez} characterizes the z component of the electron velocity, and ε_{1s}'' is the imaginary part of the solution of the dispersion equation [31] for the fields in a crystal

$$\varepsilon_{1s} = -\frac{\chi_0}{2\cos\theta_0} + \frac{c_s^2 \chi_g \chi_{-g}}{2(\alpha_B + \chi_0)\cos\theta_0}. \quad (23)$$

This expression contains two key quantities, which determine PMR and PXR, namely, the dielectric

susceptibilities $\chi_0(\omega) = \chi_{0e}(\omega_0) + \chi_{0n}(\omega)$ and $\chi_g(\omega) = \chi_{ge}(\omega_0) + \chi_{gn}(\omega)$. They each comprise an electronic (χ_{0e}, χ_{ge}) and a nuclear (χ_{0n}, χ_{gn}) contribution. The nuclear part,

$$\chi_{gn}(\omega) = -\frac{4\pi c^3}{\omega_0^2} \frac{S(\boldsymbol{g})}{V} \frac{\eta e^{-W_{LM}}}{\omega_0(1 + \alpha_c)} \frac{\Gamma/2}{(\omega - \omega_0) + i\Gamma/2}, \quad (24)$$

has a resonance character [1,35] and is responsible for the PMR. Here, $S(\boldsymbol{g})$ is the structure factor, $e^{-W_{LM}}$ the Lamb-Mössbauer factor (see the Appendix A), V the volume of the unit cell, α_c the coefficient of the internal conversion, Γ the natural linewidth of the transition and η the isotopic abundance.

The PMR becomes observable, if the parameter

$$\xi = \left| \frac{\chi_n(\omega_0)}{\chi_e(\omega_0)} \right| > 1. \quad (25)$$

By using the definition of the polarizabilities this parameter can be approximately presented as

$$\xi = \frac{\alpha^{-1} m_e}{\omega_0(1 + \alpha_c)Z}, \quad (26)$$

which can be used as a rough estimation of the excess of PMR over its electronic counterpart for various crystals, when nonforbidden reflexes are considered (with α being the fine structure constant).

IV. AVERAGING OVER THE ELECTRON BEAM PARAMETERS, MULTIPLE ELECTRON SCATTERING AND CRYSTAL MOSAICITY

The velocity distribution of experimentally available electron beams is characterized via the emittance $\epsilon_{y,z} = \Delta a \Delta \theta_{ey,z}$, with Δa the transversal and $\Delta \theta_{ey,z}$ the angular spreads. As a result, we need to average the spectral-angular emission distribution obtained for a single electron over the parameters of the entire electron beam. This is achieved by convolving the emission distribution with the electron angular distribution θ_{ey}, θ_{ez} and the initial z_0 coordinate distribution. We consider Gaussian distribution functions for the electron beam parameters given by

$$G(\theta_{ez}, \theta_{ey}, z_0) = CF(\theta_{ez}, \theta_{ey}, z_0),$$
$$F = e^{-\frac{(\theta_{ez} - \theta_{0e})^2}{\theta_s^2 + \Delta\theta_{ez}^2}} e^{-\frac{\theta_{ey}^2}{\theta_s^2 + \Delta\theta_{ey}^2}} e^{-\frac{(z_0 - a_0)^2}{\Delta a^2}}. \quad (27)$$

The constant C is a normalization constant, chosen such that the total intensity corresponds to the single electron case, i.e., $\int d\theta_{ez} d\theta_{ey} dz_0 G(\theta_{ez}, \theta_{ey}, z_0) = 1$. The angle θ_{0e} is the mean incidence angle of the electron beam on the crystal. The angle $\theta_s^2 = (E_c/E)^2(L/L_R)$ characterizes multiple electron scattering [36], with $E_c \approx 21$ MeV, L the crystal length and L_R the radiation length. For Fe, the

latter is $L_R^{Fe} = 1.757$ cm [37], for CsF $L_R^{CsF} = 2.227$ cm [37], for InSb $L_R^{InSb} = 3.701$ cm [37] and for Sc_2O_3 $L_R^{Sc_2O_3} = 5.310$ cm [37].

In addition, we perform the averaging over the beam transversal spread. For this we consider that the beam divergence is not constant along the crystal length, but is given by

$$\sigma(s) = \sqrt{\Delta a^2 + \epsilon^2 \frac{s^2}{\Delta a^2}}, \qquad -L/2 \leq s \leq L/2 \quad (28)$$

instead. Here Δa is the transversal spread in the focus center. Therefore, in the actual calculation we vary Δa in Eq. (27) from $\sigma(-L/2)$ to $\sigma(L/2)$ in $R - 1$ steps and average the resulting spectra over the resulting values, i.e., $\partial N_x/\partial x = 1/R \sum_{i=0}^{R-1} \partial N_x^i/\partial x$. Therefore, in all figures above the given value Δa corresponds to the value in the center of the focus of the beam.

The effect of crystal mosaicity influences the PMR spectrum in exactly the same way as the multiple electron scattering [17]. Consequently, we suppose that the mean square of the angles that determine the spread of crystal planes orientations is smaller than the angle θ_s—the multiple electron scattering angle.

V. RESULTS

A. Analytical estimates

Prior to discussing the realistic experimental situation, when an electron beam is characterized by an emittance we present here simple analytical formulas for the determination of the total number of photons of PMR emitted in the linewidth. For this we employ the well-known formulas of PXR [19], which were experimentally verified [21]. The number of emitted PXR photons based on the kinematic theory of diffraction can be estimated via a simple formula,

$$N_{PXR} = \alpha |\chi_g|^2 k_0 L_g, \quad (29)$$

where L_g is a coherence length. In the general case, when an electron is moving under an arbitrary angle with respect to the crystal surface the coherence length is given by an absorption length of the emitted photons. However, in the EAD geometry the coherence length is bounded by the crystal length L, $L_g \simeq L$, if the crystal length $L \leq 1$ cm. For these crystal lengths the multiple electron scattering still does not withdraw electrons from the layer with a thickness of $\sim L_{abs}$.

In addition, according to Ref. [19] the spectral width of the PXR peak is determined by the parameter

$$\Delta\omega \approx \omega_0 \sqrt{|\chi_0| + \gamma^{-2}}. \quad (30)$$

Consequently, the photon density ρ_{PXR} of PXR is approximately given by $N_{PXR}/\Delta\omega$.

Under the assumption that the frequency of the PXR peak coincides with the frequency of the resonant transition of the Mössbauer nuclei in a crystal, the number of photons which will be emitted in the spectral interval Γ per second, i.e., the number of PMR photons per second, from the beam of electrons with a current J equals

$$N_{PMR} \approx \frac{J}{e_0} \rho_{PXR} \Gamma = \alpha \frac{J}{e_0} \frac{|\chi_g|^2 k_0 L}{\sqrt{|\chi_0| + \gamma^{-2}}} \frac{\Gamma}{\omega_0}, \quad (31)$$

which provides a theoretical maximum for the emitted number of PMR photons. All averaging over parameters of the electron beam, as well as the inclusion of multiple electron scattering and temperature effects will reduce this number.

B. Numerical analysis

Coming back to a realistic situation, for our numerical analysis we choose electron beam parameters from the MAMI [21,24] experimental facility, where the experiments with PXR have been performed [21,22,24] (see Appendix B). We further consider the possibility to focus the electron beams to smaller electron beam diameters Δa, while keeping the emittance constant. Note that secondary processes and sample heating are discussed in Appendix C.

We investigated the emission from four crystals with cubic lattices. The first two are without the SMS condition: the α-iron crystal, enriched to 90% in the resonant Mössbauer isotope $^{57}_{26}Fe$ and the CsF crystal, which contains $^{133}_{55}Cs$. The last two crystals—the InSb and Sc_2O_3 crystals contain the resonant isotopes $^{121}_{51}Sb$ and $^{45}_{21}Sc$ respectively. The InSb is especially interesting since the two constituent atoms have similar charges, which allows one to specify a Bragg reflection for which the structure factors of Sb and In have equal magnitude but opposite sign, like in the SMS case. This significantly lowers PXR and provides a handle to achieve essentially background-free PMR. An analogous situation happens in the Sc_2O_3 case. The parameters used in the numerical simulation are summarized in Appendix D.

Figure 2 shows our main results, i.e., the emission spectra as a function of the dimensionless frequency x, measured in $\Gamma/2$. The parameters for the simulations of the spectra are provided in Appendixes B and D. Qualitatively, as expected from Eqs. (11) and (12), we find that the peak of the emission occurs at frequencies where the Cherenkov radiation condition is exactly fulfilled, i.e., $q' = 0$ and the maximum of the amplitude of the diffracted wave is reached ($|\alpha_B + \chi_0'|$ is minimal). The asymmetry of the distribution is caused by the fact that the contribution of the nuclear polarizability to χ_0' changes its sign when ω crosses the nuclear resonance frequency ω_0.
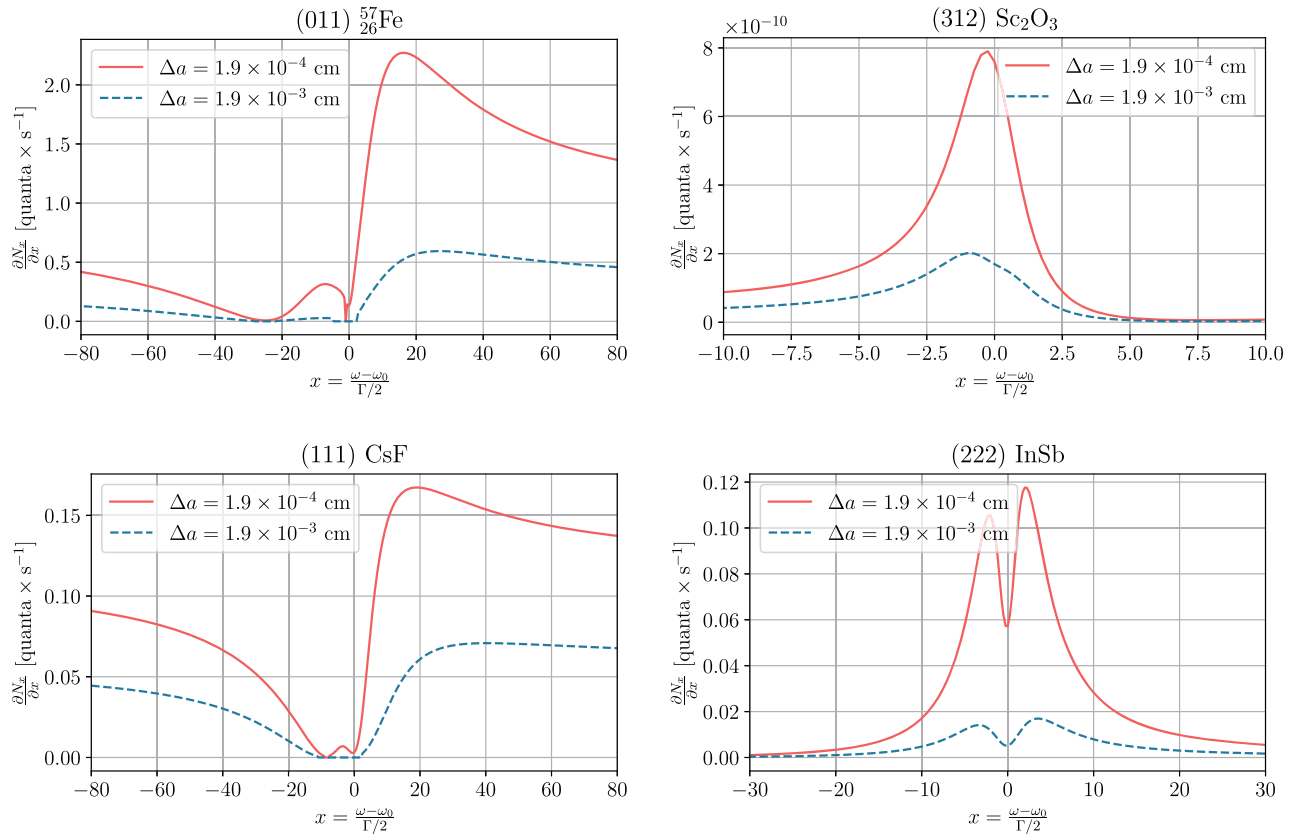
FIG. 2. The number of emitted x-ray photons per second as a function of the dimensionless frequency $x = (\omega - \omega_0)/(\Gamma/2)$. The results are averaged over the electron beam parameter distributions, for different transversal widths and divergences of the electron beam, keeping the emittance constant. The figure compares the emission from the (011) reflex of α iron (top left), the (312) reflex of Sc_2O_3 (top right), and the (111) reflex of CsF (bottom left). The bottom right panel shows pure PMR emission from the (222) reflection of the InSb crystal. For all panels, we assume an angular spread in the y direction of 10^{-3} rad. The crystal lengths are chosen as $L = 0.5$ cm. Electron parameters are chosen according to the MAMI facility, with energy $E = 1000$ MeV, vertical emittance $\epsilon = 1.9 \times 10^{-7}$ cm rad, and electron current is $j = 100\ \mu$A.

Quantitatively, for electron beams narrow in the transversal z direction ($\Delta a = 1.9 \times 10^{-4}$ cm for MAMI), our analysis predicts that the number of photons that are emitted in the spectral interval Γ ($\Delta x = 2$ in Fig. 2) near the maximum of the distribution is $N_{\mathrm{MAMI}}^{\mathrm{Fe}} = 14$ s^{-1}. For the CsF crystal, the corresponding number of photons is lower, $N_{\mathrm{MAMI}}^{\mathrm{CsF}} = 1$ cps. The reason is that the value of the ξ parameter is smaller in this case. Finally, in the case of the InSb and Sc_2O_3 crystals, one obtains $N_{\mathrm{MAMI}}^{\mathrm{InSb}} = 0.5$ s^{-1} and $N_{\mathrm{MAMI}}^{Sc_2O_3} = 2.5 \times 10^{-9}$ s^{-1} respectively.

It should be noted that in many cases the samples to be studied are superradiantly broadened (for example, spectral widths of 60 Γ have been reported in [38]). Such samples would benefit from the larger spectral width of the sources and in this case the number of resonant photons per second would be at least 10 times larger.

As expected, for InSb we find that the electronic component is strongly suppressed due to the choice of the (222) reflection, when the structure factors of In and Sb are of an opposite sign. As a result, the PMR paves the way for an essentially background-free direct spectroscopy of Sb in the energy domain.

We pay attention to the fact that the radiation formation in the EAD geometry happens in crystal layers of thickness $\sim \Delta a$. Consequently, for the radiation to be formed the crystal thickness should be larger than this value.

C. Absorption spectra with a PXR source

To illustrate the capabilities of a PXR source, in Fig. 3 we simulate the spectroscopy of α-iron with our source. We find that a well-resolved spectrum with good contrast can be achieved. The absorption spectrum is computed as

$$N(\omega_s) = N_e \int \left(\frac{I(\omega) + I(-\omega)}{2} - I_B \right)$$
$$\times e^{-k_0 D |\mathrm{Im}\chi_0(\omega - \omega_s)|} d\omega, \qquad (32)$$

where I_B is the electronic part of the intensity, $I(\omega) = \int \partial^2 N / (\partial\omega\partial\theta) G(\theta_{ez}, \theta_{ey}, z_0) d\theta_{ez} d\theta_{ey} dz_0 d\theta$ and $\chi_0(\omega - \omega_s)$ includes both the electronic and the nuclear polarizabilities.
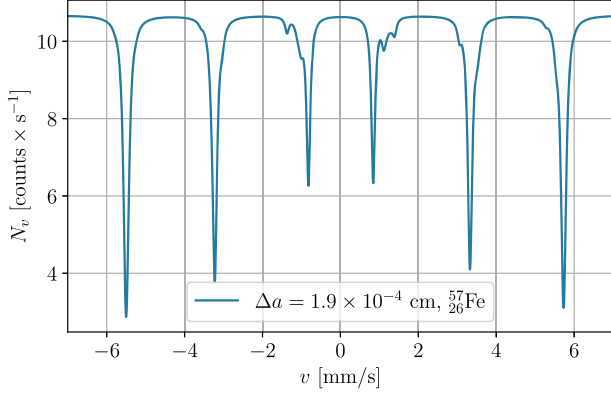
FIG. 3. Simulation of an absorption spectrum obtained with the PMR source. As a target, a nonenriched ($\eta = 0.02$) α-iron crystal of thickness $D = 5$ μm is assumed. The contrast is determined via the ratio of the electron and the nuclear contributions into the crystal polarizability near the resonance frequency and in the case of α-iron ~ 20. Other parameters are as in Fig. 2, with $\Delta a = 1.9 \times 10^{-4}$ cm. The electronic "background" is supposed to be removed via temporal gating to obtain the results.

Here N_e is the number of electrons per second. In Eq. (32), we consider that the electronic background contribution is removed from the detection signal via a temporal gating, which is possible since the nuclear emission proceeds on a much slower timescale governed by the lifetime of the nuclei.

D. Direction and divergence of the x-ray emission

Finally, we would like to briefly discuss the direction and divergence of the x-ray emission. Table I summarizes the angles characterizing the vector $\mathbf{k}$ which determines the x-ray emission direction. The actual emission is happening in the direction $\mathbf{k}' = -\mathbf{k}$. Possible values for the angles ϕ_0, ψ_0 range from $-\pi$ to π, and values for the angle θ_0 range from 0 to π. In the angular distribution of the emitted radiation two qualitatively different scales can be observed. A narrower first scale arises from the Cherenkov radiation condition. It is satisfied exactly at $q' = 0$. In this case, the angular width is defined through the coherent length L_g and the width of $q' \sim (k_0 L_g)^{-1} \sim 10^{-8}$. The second direction, which is perpendicular to q' is characterized via a variable p'. This variable is associated to the maximum of the

TABLE I. The angles θ_0, ϕ_0 of a spherical coordinate system together with the angle ψ_0, which determine the direction of emission and the orientation of the crystal with respect to the particle velocity (see Fig. 1).

Crystal	θ_0	ϕ_0	ψ_0
α-iron	107.468	−162.532	107.468
CsF	91.46	−177.94	91.55
InSb	95.91	−171.62	96.28
Sc_2O_3	101.762	−161.292	103.039

diffracted wave, and is of the order $p' \sim \sqrt{|\mathrm{Im}\chi_0|} \sim 10^{-3}$. Consequently, the PMR is concentrated around the direction given by the vector $\mathbf{k}'_0 = -\mathbf{k}_0 = (g_x + \omega_0/v, g_y, g_z)$.

Due to the finite crystal size ~ 1 mm, the beam of PMR seen by the detector has at least a width given by the crystal size, projected onto the plane defined by the vector normal to the detector. The beam divergence of order $\Delta\Omega \approx 10^{-3} \times 10^{-8}$ rad^2 is defined via the angular divergence of the emitted gamma quanta ($\simeq \gamma^{-1}$). Therefore, the target and detector should ideally be comparable or larger than the crystal size.

In addition, the angle ψ_0 is defined with respect to the central velocity v_0 of the electron beam and the divergence with respect to this direction is taken into account by the distribution function Eq. (27) and the corresponding averaging with it.

VI. CONCLUSION

In summary, we have suggested a versatile x-ray source for Mössbauer spectroscopy, based on parametric Mössbauer radiation (PMR) emitted by relativistic electrons passing through a crystal. It complements currently existing Mössbauer radiation sources due to its different qualitative properties: first, the possibility to obtain collimated photon beams without the need of x-ray optics and preliminary monochromatization of the radiation; second, this type of source is universal and can be realized for a large variety of Mössbauer crystals, including those with forbidden Bragg reflexes, thus leading to almost background free Mössbauer radiation; third, the direct conversion of electrons into resonant x-ray radiation using a cm-scale crystal invites nondedicated parasitic operation. Since our setup combining PMR with the EAD geometry operates in a thin slice of the crystal near its surface only, stacking multiple subsequent crystals could allow one to make use of thicker electron beams, or to operate multiple PXR sources in parallel from a single electron beam. Taken together, these complementary properties open perspectives for new experimental approaches with Mössbauer nuclei, in particular also for long-term, low-count rate or photon-hungry studies.

Finally, the characteristics of PMR depend only on the mass of the charged particles through the relativistic factor $\gamma^{-1} = m_0 c^2/E$. As a result, PMR-like sources as proposed here cannot only be based on electrons, but also on relativistic protons. However, to reach the same values of γ, significantly larger particle energies are required.

APPENDIX A: DEBYE-WALLER AND LAMB-MÖSSBAUER FACTORS

The effects of lattice vibrations on the crystal polarizabilities due to the temperature are determined via the Debye-Waller factor $e^{-W_{\text{DW}}} = \exp\{-1/2Z(k_g - k)\}$ for the electronic part and via the Lamb-Mössbauer factor $e^{-W_{\text{LM}}} = \exp\{-1/2[Z(k_g) + Z(k)]\}$ for the nuclear one [35]. For an isotropic crystal with a cubic lattice these factors can be estimated via the formula

$$Z(\boldsymbol{k}) = \frac{3\hbar^2|\boldsymbol{k}|^2}{8Mk_{\text{B}}\Theta_{\text{D}}} \left[1 + \frac{2\pi^2}{3}\left(\frac{T}{\Theta_{\text{D}}}\right)^2 \right], \qquad \text{(A1)}$$

which is valid for temperatures much smaller than the Debye temperature Θ_{D}. Here, where k_{B} is the Boltzmann constant and M is the mass of the resonant isotope. In order to observe the Mössbauer effect the crystal temperature should be smaller than the Debye temperature Θ_{D}. The effect of crystal heating due to the electron beam propagation and secondary processes lead to restrictions for the PMR generation which are discussed in Appendix C. These restrictions are strongest for the CsF crystal.

For α-iron the Debye temperature $\Theta_{\text{D}}^{\text{Fe}} = 470$ K, for CsF $\Theta_{\text{D}}^{\text{CsF}} = 109$ K, for InSb $\Theta_{\text{D}}^{\text{InSb}} = 163$ K and for Sc_2O_3 $\Theta_{\text{D}}^{Sc_2O_3} = 476$ K.

APPENDIX B: ELECTRON BEAM PARAMETERS

Regarding the electron beam parameters, we have investigated the MAMI [21,22,24] accelerator facility with electron beam energy 1000 MeV. The MAMI facility provides electron beams with natural vertical emittance $\epsilon = 1.9 \times 10^{-7}$ cm $\times$ rad with an electron current $j = 0.2$ μA. Under these conditions the spectrum of PXR was repeatedly studied experimentally [21,22,24]. For all simulations, the angular spread in the horizontal y direction $\Delta\theta_{ey}$ was taken to be 10^{-3} rad.

APPENDIX C: SECONDARY PROCESSES AND CRYSTAL HEATING

When an electron beam propagates inside a crystal in addition to PMR there appear many secondary processes such as bremsstrahlung and excitations of atoms of a crystal. Bremsstrahlung is mainly emitted in a small cone around an electron velocity for the case of ultrarelativistic particles. Since PMR is directed under the large angle θ_{B} to the electron velocity the bremsstrahlung radiation does not contribute to the background of PMR (please see Fig. 1). However, the bremsstrahlung quanta will be scattered on the atoms of the medium inside the channel of an accelerator, which can lead to parasitic background. Moreover the inelastic processes lead to the crystal heating. Let us estimate these two effects on the example of $^{57}_{26}$Fe.

The energy losses of electrons with the energy $E = 1$ GeV propagating in a medium according to Ref. [39] are given by

$$\frac{1}{\rho}\frac{\Delta E}{\Delta z} = 1.879 \ \frac{\text{MeV}}{\text{cm}^{-2} \times \text{g}}. \qquad \text{(C1)}$$

The density of iron equals $\rho = 7.874$ g/cm³. This yields the energy loss per unit length

$$\frac{\Delta E}{\Delta z} = 1.48 \times 10^7 \ \frac{\text{eV}}{\text{cm}} = 2.37 \times 10^{-12} \ \frac{\text{J}}{\text{cm}}. \qquad \text{(C2)}$$

Let us take the crystal length of $L = 0.5$ cm and the MAMI electron current of 100 μA. This current corresponds to $N = 6.25 \times 10^{14}$ electrons per second. As a result, for these parameters we get the total power loss

$$\Delta W = \frac{\Delta E}{\Delta z} LN \approx 740 \ \frac{\text{J}}{\text{s}}. \qquad \text{(C3)}$$

For this reason, the experiment for the observation of PMR will require cooling of the crystal, similar to high-heat-load x-ray crystal optics (see, e.g., [40]).

Now let us estimate the number of secondary particles that are produced due to bremsstrahlung that appeared from our electron beam propagating in the crystal. The power losses of the electron to produce bremsstrahlung are of the same order of magnitude as the power losses for inelastic processes [41] and for the MAMI parameters (for the Fe crystal) are

$$\Delta W_{\text{rad}} \approx \frac{EZ}{1600m_e}\Delta W \approx 1.5 \times 10^{23} \ \text{eV/s}. \qquad \text{(C4)}$$

If the electron energy $\sim$1 GeV then the average energy of bremsstrahlung quanta is $\sim$500 MeV. As a result, the number of bremsstrahlung quanta is

$$N_{\text{rad}} = 3 \times 10^{14} \ \text{quanta/s}. \qquad \text{(C5)}$$

As was already discussed the bremsstrahlung quanta are emitted mainly in the direction of the particle velocity in the ultrarelativistic case. Therefore, they are not emitted in the direction of PMR (please see Fig. 1). However, these bremsstrahlung quanta will be scattered on atoms of the medium, which is located inside the channel of a synchrotron. This will lead to the creation of background electrons that can influence the detection of PMR. Let us estimate this background.

The scattering cross section of a photon by an electron is $\sigma \approx 2\pi r_0^2$ and is weakly dependent on the energy of a photon (here $r_0 = e_0^2/m_e$ is the classical electron radius). If we consider that the channel of an accelerator is filled with a gas under high vacuum of the pressure of 1 pBar then the

characteristic concentration of electrons is $n \sim 3.87 \times 10^{11}$ cm^{-3}. Here we took the average charge of molecules of gases in the air to be ~ 14.4. As a result, we estimate the number of secondary electrons per unit length per second as

$$\frac{\Delta N_e}{\Delta L} \approx N_{rad} n \sigma \approx 0.058 \text{ electrons}/(s \times cm). \quad (C6)$$

Therefore if the characteristic length $\Delta L \sim 100$ cm we obtain the number of secondary electrons per second $N_e = 6$ electrons/s.

If we consider that the secondary electrons are isotropically distributed then in the small cone with the solid angle of 10^{-6} in which the PMR impulse is concentrated end up $\sim 6 \times 10^{-6}$ electrons/s, which is smaller than the number of photons in the PMR impulse.

Another secondary process, which we need to take into account is the nuclear recoil due to the collision with the electrons of a beam. This process can lead to the destruction of the crystal. To estimate its contribution we consider that the momentum transfer to the nucleus is determined by the average angle of the multiple electron scattering θ_s. The change of the momentum of the electron before and after the collision is given via $E\theta_s$. Here we supposed an absolutely elastic collision and ultrarelativistic electrons $|P_e| \sim E$. Consequently, the bunch of N_e electrons per second exhibits the momentum change

$$\frac{\Delta P_e}{\Delta t} \approx E \theta_s N_e. \quad (C7)$$

We now consider that this momentum is uniformly transferred to the nuclei of the crystal in the region of the volume $(L\theta_s)^2 \times L$ where the electrons propagate. Consequently, we can write the following expression for the change in momentum ΔP_{nuc} of a single nucleus:

$$\rho_{nuc} \theta_s^2 L^3 \Delta P_{nuc} \approx E \theta_s N_e \Delta t, \quad (C8)$$

where ρ_{nuc} is the number of nuclei in the unit volume of the crystal.

The energy of the nucleus of a mass M during the time interval Δt is expressed accordingly:

$$\Delta E_{nuc} \approx \frac{(\Delta P_{nuc})^2}{2M} \approx \frac{E^2}{2M\theta_s^2} \frac{(N_e \Delta t)^2}{L^6 \rho_{nuc}^2}. \quad (C9)$$

As a result for the crystal $^{57}_{26}$Fe and for the MAMI experimental conditions we find the final estimation for the temperature increase of the crystal due to nuclear recoil,

$$\Delta T[K] \approx 3.1(\Delta t[s])^2, \quad (C10)$$

which becomes comparable with the Debye temperature during the time $\Delta t \approx 12$ s. We also mention that the realistic time interval will be larger since the provided

estimation does not take into account the thermal conductivity of the crystal.

We want to stress here that the proposed experimental conditions for the observation of PMR are coincident with the conditions under which the PXR was experimentally observed [21,22,24]. Since in the PXR experiments the crystal was not destroyed we consider that the crystal will not be destroyed in the proposed experiment for the observation of the PMR.

APPENDIX D: CRYSTAL PARAMETERS

We choose the most intense reflection for the α-iron crystal, namely, the (011) reflection. For this reflection we employ the following parameters, taken from the x-ray database [42]:

$$\hbar\omega_B = 14.41 \text{ keV}, \qquad k_0 = 7.35 \times 10^8 \text{ cm}^{-1},$$
$$\chi'_{0e} = -0.15 \times 10^{-4}, \qquad \chi''_{0e} = 0.69 \times 10^{-6},$$
$$\chi'_{ge} = -0.10 \times 10^{-4}, \qquad \chi''_{ge} = 0.67 \times 10^{-6}. \quad (D1)$$

The α-iron crystal has cubic crystalline structure with interplanes distance $d = 2.87 \times 10^{-8}$ cm. In addition, we assume it to be enriched to 90% (the isotopic abundance $\eta = 0.9$) with the resonant Mössbauer isotope $^{57}_{26}$Fe, which has the natural decay width $\Gamma = 4.66 \times 10^{-12}$ keV. The coefficient of internal conversion $\alpha_C = 8.56$ and the structure factor $S(\boldsymbol{g}) = 2$ for $^{57}_{26}$Fe.

For CsF, we employ the (111) reflection with the parameters [42]

$$\hbar\omega_B = 80.997 \text{ keV}, \qquad k_0 = 4.10 \times 10^9 \text{ cm}^{-1},$$
$$\chi'_{0e} = -0.25 \times 10^{-6}, \qquad \chi''_{0e} = 0.42 \times 10^{-8},$$
$$\chi'_{ge} = -0.15 \times 10^{-6}, \qquad \chi''_{ge} = 0.39 \times 10^{-8}. \quad (D2)$$

The CsF crystal has a cubic crystalline structure with interplanar distance $d = 6.008 \times 10^{-8}$ cm. The natural decay width of the $^{133}_{55}$Cs isotope is $\Gamma = 72.77 \times 10^{-12}$ keV, the internal conversion coefficient $\alpha_C = 1.72$, the structure factor $S(\boldsymbol{g}) = 4$ and isotopic abundance $\eta = 1$.

For InSb, we employ the (222) reflection with the parameters [42]

$$\hbar\omega_B = 37.133 \text{ keV}, \qquad k_0 = 1.88 \times 10^9 \text{ cm}^{-1},$$
$$\chi'_{0e} = -0.15 \times 10^{-5}, \qquad \chi''_{0e} = 0.72 \times 10^{-7},$$
$$\chi'_{ge} = 0.17 \times 10^{-7}, \qquad \chi''_{ge} = -0.46 \times 10^{-8}. \quad (D3)$$

The InSb crystal has cubic crystalline structure with interplanar distance $d = 6.4789 \times 10^{-8}$ cm. The isotope $^{121}_{51}$Sb has a natural decay width $\Gamma = 0.13 \times 10^{-6}$ eV, the internal conversion coefficient $\alpha_C = 11.11$. The structure

factors are $S(\boldsymbol{g}) = -4$ for $^{121}_{51}$Sb and $S(\boldsymbol{g}) = 4$ for $_{49}$In. The isotopic abundance $\eta = 0.5725$.

For Sc$_2$O$_3$, we employ the (312) reflection with the parameters [42]

$$\hbar\omega_{\mathrm{B}} = 12.40 \text{ keV}, \qquad k_0 = 6.28 \times 10^8 \text{ cm}^{-1},$$
$$\chi'_{0\mathrm{e}} = -0.10 \times 10^{-4}, \qquad \chi''_{0\mathrm{e}} = 0.22 \times 10^{-6},$$
$$\chi'_{\boldsymbol{g}\mathrm{e}} = 0.67 \times 10^{-7}, \qquad \chi''_{\boldsymbol{g}\mathrm{e}} = 0.22 \times 10^{-7}. \qquad \text{(D4)}$$

The Sc$_2$O$_3$ crystal has cubic crystalline structure with interplanar distance $d = 9.21 \times 10^{-8}$ cm. The isotope $^{45}_{21}$Sc has a natural decay width $\Gamma = 1.4 \times 10^{-15}$ eV, the internal conversion coefficient $\alpha_{\mathrm{C}} = 400$. The structure factors are $S(\boldsymbol{g}) = 3.415$ for $^{45}_{21}$Sc and $S(\boldsymbol{g}) = -10.566$ for $_8$O. The isotopic abundance $\eta = 1$.

---

[1] R. Röhlsberger, *Nuclear Condensed Matter Physics with Synchrotron Radiation*, edited by G. Höhler, J. H. Kühn, T. Müller, J. Trümper, A. Ruckenstein, P. Wölfle, and F. Steiner, Springer Tracts in Modern Physics Vol. 208 (Springer-Verlag, Berlin, 2005).

[2] *The Rudolf Mössbauer Story*, edited by M. Kalvius and P. Kienle (Springer-Verlag, Berlin, 2012).

[3] R. Rüffer and A. I. Chumakov, Nuclear resonance, in *Synchrotron Light Sources and Free-Electron Lasers*, edited by E. J. Jaeschke, S. Khan, J. R. Schneider, and J. B. Hastings (Springer International Publishing, Cham, 2016), pp. 1759–1795.

[4] B. Adams *et al.*, Scientific opportunities with an x-ray free-electron laser oscillator, arXiv:1903.09317.

[5] K. P. Heeg, A. Kaldun, C. Strohm, P. Reiser, C. Ott, R. Subramanian, D. Lentrodt, J. Haber, H.-C. Wille, S. Goerttler, R. Rüffer, C. H. Keitel, R. Röhlsberger, T. Pfeifer, and J. Evers, Spectral narrowing of x-ray pulses for precision spectroscopy with nuclear resonances, Science **357**, 375 (2017).

[6] A. Q. R. Baron, Introduction to high-resolution inelastic x-ray scattering, arXiv:1504.01098.

[7] B. W. Adams, C. Buth, S. M. Cavaletto, J. Evers, Z. Harman, C. H. Keitel, A. Pálffy, A. Picón, R. Röhlsberger, Y. Rostovtsev, and K. Tamasaku, X-ray quantum optics, J. Mod. Opt. **60**, 2 (2013).

[8] R. Röhlsberger, J. Evers, and S. Shwartz, Quantum and nonlinear optics with hard x rays, in *Synchrotron Light Sources and Free-Electron Lasers*, edited by E. J. Jaeschke, S. Khan, J. R. Schneider, and J. B. Hastings (in Ref. [3]), pp. 1197–1229.

[9] E. Kuznetsova and O. Kocharovskaya, Quantum optics with x rays, Nat. Photonics **11**, 685 (2017).

[10] S. L. Ruby, Mössbauer experiments without conventional sources, J. Phys. (Paris), Colloq. **35**, C6 (1974).

[11] E. Gerdau, R. Rüffer, H. Winkler, W. Tolksdorf, C. P. Klages, and J. P. Hannon, Nuclear Bragg Diffraction of Synchrotron Radiation in Yttrium Iron Garnet, Phys. Rev. Lett. **54**, 835 (1985).

[12] G. V. Smirnov, U. van Bürck, A. I. Chumakov, A. Q. R. Baron, and R. Rüffer, Synchrotron Mössbauer source, Phys. Rev. B **55**, 5811 (1997).

[13] R. Masuda, T. Mitsui, S. Kitao, S. Higashitaniguchi, Y. Yoda, and M. Seto, Development of neV-resolution spectroscopy using synchrotron-based ^{57}Fe Mössbauer radiation, Jpn. J. Appl. Phys. **47**, 8087 (2008).

[14] M. Seto, R. Masuda, S. Higashitaniguchi, S. Kitao, Y. Kobayashi, C. Inaba, T. Mitsui, and Y. Yoda, Synchrotron-Radiation-Based Mössbauer Spectroscopy, Phys. Rev. Lett. **102**, 217602 (2009).

[15] V. Potapkin, A. I. Chumakov, G. V. Smirnov, J.-P. Celse, R. Rüffer, C. McCammon, and L. Dubrovinsky, The 57fe synchrotron Mössbauer source at the ESRF, J. Synchrotron Radiat. **19**, 559 (2012).

[16] P. Alexeev, O. Leupold, I. Sergueev, M. Herlitschke, D. F. McMorrow, R. S. Perry, E. C. Hunter, R. Röhlsberger, and H.-C. Wille, Nuclear resonant scattering from 193ir as a probe of the electronic and magnetic properties of iridates, Sci. Rep. **9**, 5097 (2019).

[17] V. G. Baryshevsky, I. D. Feranchuk, and A. P. Ulyanenkov, *Parametric X-Ray Radiation in Crystals: Theory, Experiment and Applications (Springer Tracts in Modern Physics)* (Springer, New York, 2006).

[18] V. G. Baryshevsky, I. D. Feranchuk, A. O. Grubich, and A. V. Ivashin, Theoretical interpretation of parametric x-ray spectra, Nucl. Instrum. Methods Phys. Res., Sect. A **249**, 306 (1986).

[19] I. D. Feranchuk and A. V. Ivashin, Theoretical investigation of the parametric x-ray features, J. Phys. (Paris) **46**, 1981 (1985).

[20] V. G. Baryshevsky and I. D. Feranchuk, Parametric x-rays from ultrarelativistic electrons in a crystal: Theory and possibilities of practical utilization, J. Phys. (Paris) **44**, 913 (1983).

[21] K. H. Brenzinger, C. Herberg, B. Limburg, H. Backe, S. Dambach, H. Euteneuer, F. Hagenbuck, H. Hartmann, K. Johann, K. H. Kaiser, O. Kettig, G. Knies, G. Kube, W. Lauth, H. Schöpe, and T. Walcher, Investigation of the production mechanism of parametric x-ray radiation, Z. Phys. A **358**, 107 (1997).

[22] K.-H. Brenzinger, B. Limburg, H. Backe, S. Dambach, H. Euteneuer, F. Hagenbuck, C. Herberg, K. H. Kaiser, O. Kettig, G. Kube, W. Lauth, H. Schöpe, and T. Walcher, How Narrow is the Linewidth of Parametric X-ray Radiation?, Phys. Rev. Lett. **79**, 2462 (1997).

[23] J. Hyun, M. Satoh, M. Yoshida, T. Sakai, Y. Hayakawa, T. Tanaka, K. Hayakawa, I. Sato, and K. Endo, Compact and intense parametric x-ray radiation source based on a linear accelerator with cryogenic accelerating and decelerating copper structures, Phys. Rev. Accel. Beams **21**, 014701 (2018).

[24] W. Lauth, H. Backe, O. Kettig, P. Kunz, A. Sharafutdinov, and T. Weber, Coherent x-rays at MAMI, Eur. Phys. J. A **28**, 185 (2006).

[25] B. Sones, Y. Danon, and R. Block, Lithium fluoride (lif) crystal for parametric x-ray (pxr) production, Nucl. Instrum. Methods Phys. Res., Sect. B **227**, 22 (2005).

[26] V. V. Morokhovskii, K. H. Schmidt, G. Buschhorn, J. Freudenberger, H. Genz, R. Kotthaus, A. Richter,

M. Rzepka, and P. M. Weinmann, Polarization of Parametric X Radiation, Phys. Rev. Lett. **79,** 4389 (1997).

[27] J. Freudenberger, H. Genz, V. V. Morokhovskyi, A. Richter, and J. P. F. Sellschop, Parametric X Rays Observed Under Bragg Condition: Boost of Intensity by a Factor of Two, Phys. Rev. Lett. **84,** 270 (2000).

[28] A. Ahmadi and I. D. Feranchuk, Parametric γ-radiation from electrons in Mössbauer crystal, Eur. Phys. J. Appl. Phys. **62,** 10702 (2013).

[29] A. Ahmadi and I. D. Feranchuk, Increase of parametric x-ray intensity due to the Borrmann effect, Nucl. Instrum. Methods Phys. Res., Sect. B **311,** 78 (2013).

[30] O. D. Skoromnik, V. G. Baryshevsky, A. P. Ulyanenkov, and I. D. Feranchuk, Radical increase of the parametric x-ray intensity under condition of extremely asymmetric diffraction, Nucl. Instrum. Methods Phys. Res., Sect. B **412,** 86 (2017).

[31] O. D. Skoromnik, I. D. Feranchuk, and D. V. Lu, Parametric x-ray radiation in the Smith-Purcell geometry for nondestructive beam diagnostics, Nucl. Instrum. Methods Phys. Res., Sect. B **444,** 125 (2019).

[32] A. Authier, *Dynamical Theory of X-ray Diffraction*, International Union of Crystallography Monographs on Crystallography (Oxford University Press, New York, 2001).

[33] M. Born and E. Wolf, *Principles of Optics: Electromagnetic Theory of Propagation, Interference and Diffraction of Light* (Elsevier Science, New York, 2013).

[34] MAX IV authors, MAX IV Synchrotron Facility. Parameters, https://www.maxiv.lu.se/accelerators-beamlines/accelerators/accelerator-documentation/3-gev-storage-ring/.

[35] A. M. Afanas'ev and Y. Kagan, Suppression of inelastic channels in resonant nuclear scattering in crystals, Sov. Phys. JETP **21,** 215 (1965).

[36] M. Ter-Mikaelian, *High-Energy Electromagnetic Processes in Condensed Media*, Interscience Tracts on Physics and Astronomy (Wiley-Interscience, New York, 1972).

[37] M. Tanabashi *et al.* (Particle Data Group), Review of particle physics, Phys. Rev. D **98,** 030001 (2018).

[38] R. Rohlsberger, K. Schlage, B. Sahoo, S. Couet, and R. Ruffer, Collective Lamb shift in single-photon superradiance, Science **328,** 1248 (2010).

[39] *Studies in Penetration of Charged Particles in Matter* (National Academies Press, Washington, DC, 1964).

[40] A. I. Chumakov, I. Sergeev, J.-P. Celse, R. Rüffer, M. Lesourd, L. Zhang, and M. S. del Río, Performance of a silicon monochromator under high heat load, J. Synchrotron Radiat. **21,** 315 (2014).

[41] E. Lifshitz and L. Pitaevskij, *Relativistic Quantum Theory*, Lev D. Landau: Course of Theoretical Physics No. 2 (Pergamon, New York, 1974).

[42] S. A. Stepanov, X-ray dynamical diffraction web server, http://x-server.gmca.aps.anl.gov/.